**Supporting Information**

# Direct Observation of the Formation Pathway of [$Mo_{132}$] Keplerates

*Subharanjan Biswas,[1] Dolores Melgar,[2,3] Amitava Srimany,[4] Antonio Rodríguez-Fortea,[5] Thalappil Pradeep,*[4] Carles Bo,*[2] Josep M. Poblet*[5] and Soumyajit Roy*[1]*

1 Eco-Friendly Applied Materials Laboratory (EFAML), Materials Science Centre, Department of Chemical Sciences, Indian Institute of Science Education and Research-Kolkata (IISER-Kolkata), Mohanpur Campus, Mohanpur-741246, India, Email- s.roy@iiserkol.ac.in

2 Institute of Chemical Research of Catalonia (ICIQ), Av. Països Catalans 16, 43007 Tarragona, Spain, Email- cbo@iciq.cat

3 Departament d'Enginyeria Química, ETSEQ, Universitat Rovira i Virgili, Av. dels Països Catalans, 26, 43007 Tarragona, Spain

4 Department of Chemistry, Indian Institute of Technology Madras, Chennai 600036, India, Email- pradeep@iitm.ac.in

5 Departament de Química Física i Inorgànica, Universitat Rovira i Virgili, Marcel·lí Domingo 1, 43007 Tarragona, Spain, Email- josepmaria.poblet@urv.cat

**Calculations on the dinuclear species $[HMo^{V}_{2}O_{6}(CH_{3}COO)(H_{2}O)_{2}]^{-}$**

Once the system, heptamolybdate in aqueous solution, is reduced a peak assigned to the formula $[HMo^{V}_{2}O_{6}(CH_{3}COO)(H_{2}O)_{2}]^{-}$ appears in the mass spectrum. The first problem that we encounter is that the assignament of the oxidation states is incompatible with the total charge of the molecule. If the two Mo atoms are Mo(V), the charge of the system should be 2−. So, for this charge to be correct, one should have (i) a reduced Mo(V) and a totally oxidized Mo(VI); or (ii) an extra proton in the formula. In order to clarify this point, we have made computations on different model systems [standard settings: ADF, BP86/TZP with COSMO], as shown in Table S1. The hypothetical mixed-valence dimer $[Mo^{V}Mo^{VI}O_{5}(OH)(CH_{3}COO)(H_{2}O)_{2}]^{-}$ (**1**) with the two Mo ions hexacoordinated in an octahedral environment with two oxo bridges, two aqua ligands, a hydroxo ligand and a carboxylato keeps the structure after geometry optimization (first row, Table S1). The Mo···Mo distance is 3.098 Å. The same dinuclear compound with 2− charge, i.e. the two metal ions as Mo(V), leads to a structure where one Mo(V) ion has lost one aqua ligand, which remains hydrogen-bonded to the system (second row, Table S1). The Mo···Mo distance is in this reduced state somewhat shorter (3.070 Å) than for **1** due to the presence of two, instead of one, electrons in the bonding Mo−Mo orbital. To keep the 1− charge with two Mo(V) ions, one extra $H^{+}$ has to be added to the structure (model compound **3**). Optimization of model **3** leads to important structural changes where the two Mo(V) ions are singly bridged and their coordination environments have changed to five and four (third row, Table S1). The structural isomer $[Mo^{V}_{2}O_{2}(OH)_{6}(CH_{3}COO)]^{-}$ (**4**), with no aqua ligands and six hydroxo ligands, however, keeps the octahedral environment around each Mo(V) ion (fourth row, Table S1). The Mo···Mo is now significantly decreased to 2.727 Å.

| Species | Coord $(Mo1)_{init}$ | Coord $(Mo2)_{init}$ | Coord $(Mo1)_{fin}$ | Coord $(Mo2)_{fin}$ |
|---|---|---|---|---|
| $[Mo^{V}Mo^{VI}O_5(OH)(CH_3COO)(H_2O)_2]^-$ (**1**) | 6 [3O/1OH/1w/1c] | 6 [4O/1w/1c] | 6 [3O/1OH/1w/1c] | 6 [4O/1w/1c] |
| $[Mo^{V}_2O_5(OH)(CH_3COO)(H_2O)_2]^{2-}$ (**2**) | 6 [3O/1OH/1w/1c] | 6 [3O/1OH/1w/1c] | 5 [3O/1OH/1c] | 6 [4O/1w/1c] |
| $[Mo^{V}_2O_4(OH)_2(CH_3COO)(H_2O)_2]^-$ (**3**) | 6 [3O/1OH/1w/1c] | 6 [4O/1w/1c] | 5 [1O/2OH/1c] | 4 [2O/2OH] |
| $[Mo^{V}_2O_2(OH)_6(CH_3COO)^-$ (**4**) | 6 [2O/3OH/1c] | 6 [2O/3OH/1c] | 6 [2O/3OH/1c] | 6 [2O/3OH/1c] |

Table S1**.** Results for the geometry optimizations at BP86/TZP level using COSMO (water as solvent) done on model systems related to the $[HMo^{V}_2O_6(CH_3COO)(H_2O)_2]^-$ assignation of the mass spectrum. The nomenclature for ligands is the following O: oxo; OH: hydroxo; w: water; c: carboxylate.

**Car-Parrinello molecular dynamics on $[Mo^{V}_2O_2(OH)_6(CH_3COO)]^-$**

We have performed Car-Parrinello molecular dynamics (MD) simulations, using the CPMD code.[1] The description of the electronic structure is based on the expansion of the valence electronic wave functions into a plane wave (PW) basis set, which is limited by an energy cutoff of 70 Ry. The interaction between the valence electrons and the ionic cores is treated through the pseudopotential (PP) approximation. Norm-conserving Martins-Troullier PPs are employed.[2] A semicore Mo PP was used according to the work of Boero et al.[3] We adopt the generalized gradient-corrected functionals of Becke for the exchange and of Perdew for the correlation.[4-6] In the MD simulations, the wave functions are propagated in the Car-Parrinello scheme, by integrating the equations of motion derived from the extended Car-Parrinello Lagrangian.[7] We use a time step of 0.144 fs and a fictitious electronic mass of 900 a.u. A Nosé-Hoover thermostat keeps the temperature around 300 K.[8-10]

The cell box that contains one $[Mo^{V}_{2}O_{2}(OH)_{6}(CH_{3}COO)]^{-}$ dimer and 58 water molecules (a = b = c = 12.58 Å) is repeated periodically in the space by the standard periodic boundary conditions. After 3 ps of equilibration, the initial structure of the $Mo^{V}$ dimer (see fourth row of Table S1) is somewhat changed; there is only one oxo bridge between the two $Mo^{V}$ ions and an intramolecular proton transfer has taken place. Hence, one $Mo^{V}$ ion is six-coordinated [2O/2OH/1w/1c] and the other is five-coordinated [2O/2OH/1c]. We have performed a production run of 26 ps. Figure 3B shows the Mo−O radial distribution functions and their integrations, which yield the total coordination number, for each $Mo^{V}$ ion.

The sharp spikes at around 1.75 Å, which integrate one O atom for each Mo ion, are attributed to the terminal oxo ligands. The peaks at around 2 Å, which integrate up to four atoms, correspond to the hydroxo and the bridging oxo ligands. The peaks and shoulders at distances between 2 and 2.5 Å are due to the aqua and carboxylato ligands. At distances between 2.5 and 3 Å the Mo−O coordination number shows a plateau associated with the presence of five O atoms in the coordination sphere of Mo(1). On the other hand, Mo(2) is six-coordinated. Therefore, the coordination sphere for each of the two $Mo^{V}$ ions is mainly kept during the whole simulation. Other shallow maxima appear at distances larger than 3 Å, which are associated to the first solvation sphere and to the rest of the O atoms that belong to the cluster. Figure S1 shows the evolution of the coordination environment for each of the $Mo^{V}$ ions. The carboxylato ligand, which is always coordinated to at least one of the two $Mo^{V}$ ions, is counted as an oxo ligand. Significant changes in the number of oxo, hydroxo and aqua ligands during the simulation, keeping almost constant the total number of ligands to five for Mo(1) and six to Mo(2), are observed as a consequence of intramolecular dimer-to-dimer and intermolecular solvent-to-dimer proton transfers. Figure S2 shows the evolution of the number of H atoms bonded to the O atoms directly coordinated to the Mo ions. The initial total number of six is mainly kept for almost the whole simulation; however, a seventh

proton is observed to attach to the dimer in the last part of the simulation (after 20 ps). The changes in the number of H atoms bound to Mo(1) or Mo(2) also denote the high mobility of protons within the dimer.

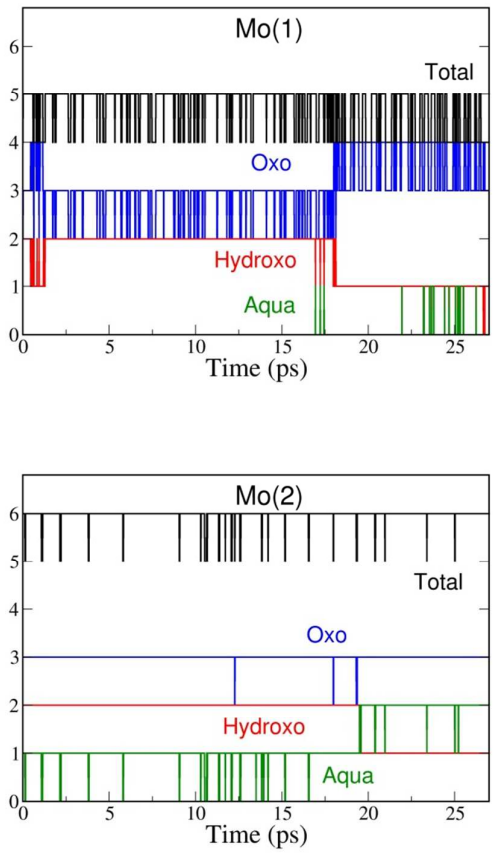


Figure S1. Number of oxo (blue), hydroxo (red) and aqua (green) ligands as well as the total number of ligands (black) for each of the Mo ions during the 27 ps of simulation starting from $[Mo^{V}_{2}O_{2}(OH)_{6}(CH_{3}COO)]^{-}$. The carboxylato bridge is considered as an oxo ligand.

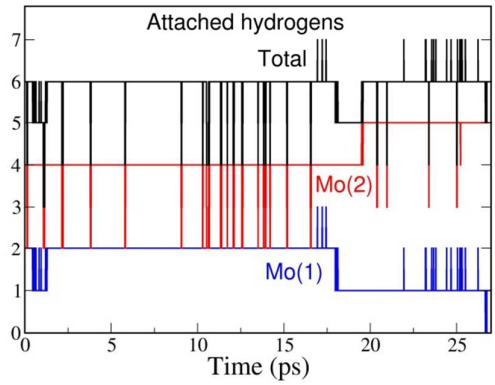


Figure S2. Number of hydrogen atoms bonded to oxygen atoms that are directly coordinated to Mo(1) (blue) and Mo(2) (red) as well as their total number (sum, in black) during the 27 ps of simulation starting from $[Mo^{V}_{2}O_{2}(OH)_{6}(CH_{3}COO)]^{-}$.

Finally, we have analyzed in more detail the fate of the carboxylato ligand during the dynamics. We have found (see Figure S3) that it is a rather labile ligand that is not always bonded to the two Mo ions at the same time. However, it is always attached to at least one of the Mo ions during the 27 ps of simulation. The carboxylato ligand is rather strongly bonded to Mo(2) with distances that are smaller than 2.5 Å for the whole simulation; it is, however, more weakly bonded to Mo(1) with longer Mo−O distances that oscillate around 2.5 Å and sometimes are larger than 2.8 Å.

Our results show that the dynamical description of the system is necessary to fully understand its properties and behavior.

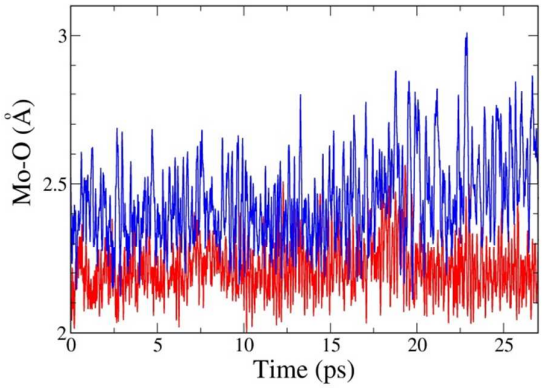


Figure S3. Mo−O(carboxylato) distances, blue line for Mo(1) and red line for Mo(2), during the 27 ps of simulation starting from $[Mo^{V}_{2}O_2(OH)_6(CH_3COO)]^{-}$.

**Car-Parrinello molecular dynamics on $[Mo_7O_{24}]^{6-}$ and the reduced system $[Mo_7O_{24}]^{7-}$**

Car-Parrinello MD simulations were performed with a cell box containing one heptamolybdate $[Mo_7O_{24}]^{6-}$, 140 water molecules, two hydronium $H_3O^+$ and two ammonium $NH_4^+$ cations (a = b = c = 16.90 Å). During the equilibration (1 ps), the heptamolybdate gets protonated in a terminal oxo ligand. After 3 ps of simulation, the heptamolybdate remains essentially singly protonated with the seven Mo atoms keeping their octahedral coordination.

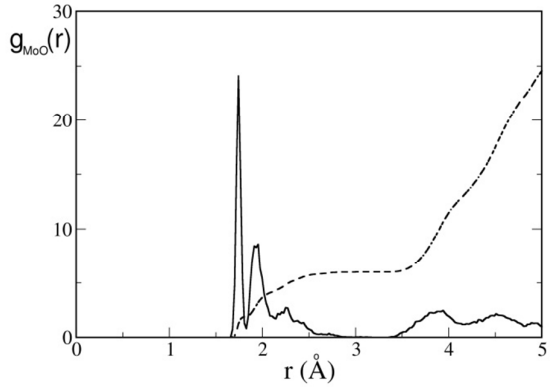


Figure S4. Mo−O radial distribution function (solid line) and its integration, the coordination number (broken line), of Mo for 3 ps of simulation starting from $[Mo_7O_{24}]^{6-}$.

The sharp spike at around 1.75 Å, attributed to the terminal oxo ligands, integrates two oxygen atoms per Mo. The spike at around 2 Å, which integrates on average two O atoms per Mo, corresponds mainly to the bridging $\mu_2$-oxo ligands. The shallower peak at around 2.25 Å, which also integrates two O atoms, corresponds to the $\mu_3$- and $\mu_4$-oxo ligands that are in *trans* with respect to the terminal oxo ligands. Figure S5 shows that the hydroxo ligand present initially in the heptamolybdate complex is kept during the dynamics; at some point, a proton of the solution is eventually attached to the molybdate.

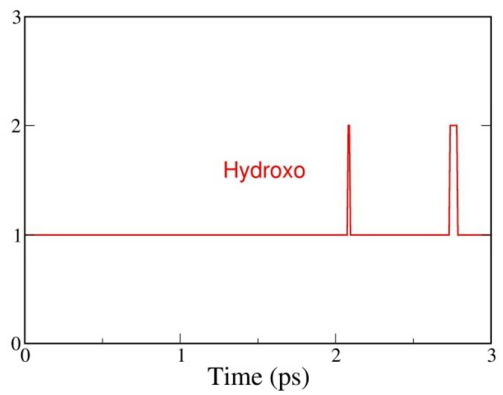


Figure S5. Number of hydroxo ligands in the $[Mo_7O_{24}]^{6-}$ heptamolybdate during the 3 ps of simulation.

We have finally performed Car-Parrinello MD simulations in the reduced open-shell $[Mo_7O_{24}]^{7-}$ heptamolybdate in order to understand the initial steps in the formation of the $Mo_{132}$ Keplerate, which takes place after reduction of the reactant $[Mo_7O_{24}]^{6-}$. The same simulation box as in the totally oxidized heptamolybdate is used. After 1.6 ps of equilibration, a production run of 4.8 ps is analyzed. During this short time scale, we observe that the singly reduced heptamolybdate complex is rather stable and keeps its initial structure with the seven molybdate ions having octahedral coordination. Figure S6 shows that the

Mo−O radial distribution function for the reduced $[Mo_7O_{24}]^{7-}$ (red line) is quite similar to that of the oxidized $[Mo_7O_{24}]^{6-}$ complex (blue line). A slight difference can be observed in the region around 2 Å, which corresponds mainly to the bridging $\mu_2$-oxo ligands, where the second spike is somewhat displaced to longer distances for the reduced system compared to the oxidized one. Moreover, the third peak observed for $[Mo_7O_{24}]^{6-}$ at around 2.25 Å is split in two small peaks for $[Mo_7O_{24}]^{7-}$. So, a slight expansion of some bonds in the coordination sphere of the Mo ions seem to happen at this short time scale.

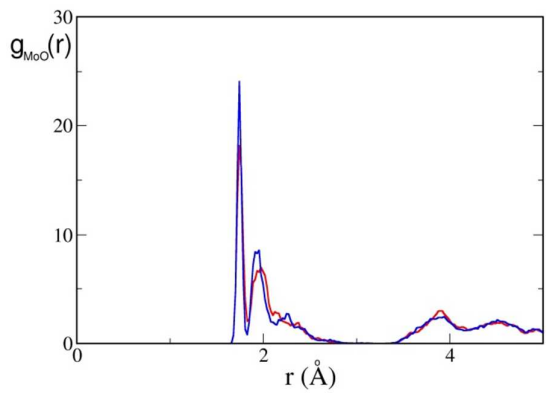


Figure S6. Mo−O radial distribution functions for the reduced $[Mo_7O_{24}]^{7-}$ (red line) and the oxidized $[Mo_7O_{24}]^{6-}$ (blue line) heptamolybdates.

Figure S7 shows the number of hydroxo ligands in the reduced heptamolybdate during the simulation. The initial hydroxo group is kept during the whole trajectory and for some short periods, especially at around 1 ps, other protons are eventually attached to the molybdate. The larger changes in the number of hydroxo groups of the reduced $[Mo_7O_{24}]^{7-}$ along the trajectory denotes that protons interact more easily with the heptamolybdate once it is reduced.

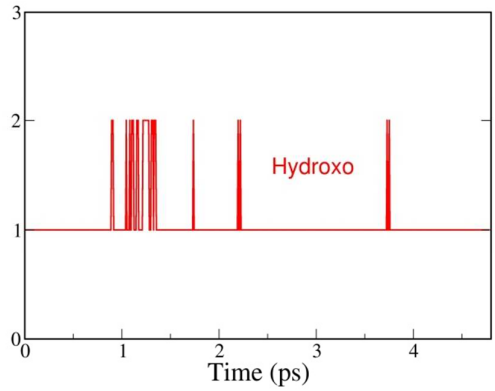


Figure S7. Number of hydroxo ligands in the reduced $[Mo_7O_{24}]^{7-}$ heptamolybdate during the 4.8 ps of simulation.

The evolution of the Mo−O distances of the eight $\mu_4$-oxo ligands for the oxidized and the reduced heptamolybdates along the time is plotted in Figure S8. A small expansion of some of these distances is observed when going from the oxidized to the reduced molybdate, especially for the smallest ones (black lines in Figure S8), which are the Mo−O distances that are in *trans* position with respect to the terminal hydroxo ligands (average values for the oxidized and reduced systems: 1.965 *vs* 2.043 Å). So, we can conclude that, at this short time scale, the reduced heptamolybdate is rather stable in good agreement with the fact that it does not evolve rapidly to the $Mo_{132}$ Keplerate (the reaction takes some hours). However, a small expansion of the coordination sphere of Mo can be observed after reduction of the heptamolybdate.

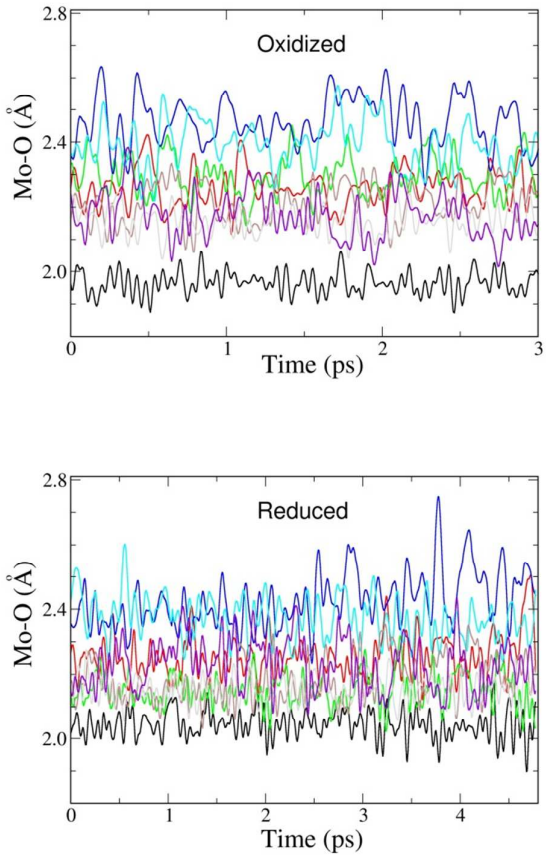


Figure S8. Mo−O distances of the eight $\mu_4$-oxo ligands for the oxidized $[Mo_7O_{24}]^{6-}$ and reduced $[Mo_7O_{24}]^{7-}$ heptamolybdates during the Car-Parrinello simulations.

**Condensation Energies from Pentagonal and Linker Unit Model**

All molecular geometries were fully optimized without constraints by using the Amsterdam Density Functional (ADF2012) program[11] developed by Baerends, Ziegler, and co-workers. We used a GGA BP86 functional and a triple-ζ plus one polarization function basis set. Relativistic corrections were introduced by means of the scalar-relativistic zero-order regular approximation (ZORA).[12,13] Solvent effects were taken into account on the basis of the continuous solvent model COSMO[14]] with default radii.

| | | | | | | |
|---|---|---|---|---|---|---|
| | -21.1 | -44.1 | -74.6 | -72.5 | -155.1 | -172.8 |
| | $4OH^-$ | $3OH^-$ | $2OH^-$ | $2OH^-$ | $OH^-$ | $2H_2O$ |
| | -2.6 | -25.6 | -56.1 | -54.0 | -102.8 | -97.1 |
| | $3OH^-$ | $2OH^-$ | $OH^-$ | $OH^-$ | $2H_2O$ | $H_3O^+$ |
| | 25.7 | 2.8 | -27.8 | -25.7 | -17.4 | -11.7 |
| | $2OH^-$ | $OH^-$ | $2H_2O$ | $2H_2O$ | $H_3O^+$ | $2H_3O^+$ |
| | 16.2 | -6.8 | -37.3 | -35.2 | -27.0 | -21.2 |
| | $2OH^-$ | $OH^-$ | $2H_2O$ | $2H_2O$ | $H_3O^+$ | $2H_3O^+$ |
| | 24.5 | 1.5 | 28.1 | 30.2 | 38.5 | 44.2 |
| | $OH^-$ | $2H_2O$ | $H_3O^+$ | $H_3O^+$ | $2H_3O^+$ | $3H_3O^+$ |
| | -28.9 | 5.3 | 31.9 | 34.0 | 42.3 | 48.0 |
| | $2H_2O$ | $H_3O^+$ | $2H_3O^+$ | $2H_3O^+$ | $3H_3O^+$ | $4H_3O^+$ |

Table S2. Condensation reaction energies (in kcal/mol) between dimers (rows) and pentagonal (columns) fragments as function of the protonation degree. The inner labels indicate the products obtained upon condensation.

We computed the condensation reaction energy between a dimer and pentagon moieties as function of the protonation degree. These results are collected in Table S2. For each unit, we considered different level of protonation, i.e., from having no protons to having four protons. This scenario aims at simulating basic and acidic conditions, respectively. Note that the values for situations corresponding to low pH, in the bottom-right part of the table, are all positive, indicating unstable products. Those values for high pH, top-left, are all negative thus indicating favorable reactions. It is interesting to note that the most favorable values correspond, in all the cases, to situations having four protons in all, which are those situations

that give water as product. These numbers demonstrate that the two building blocks, a linker and a pentagon, can condensate only under certain pH conditions.

| | | | |
|---|---|---|---|
| | 110.3 | 72.8 | 5.2 |
| | $3OH^-$ | $2OH^-$ | $OH^-$ |
| | 61.6 | 26.4 | -11.8 |
| | $2OH^-$ | $OH^-$ | $2H_2O$ |
| | 15.8 | -12.0 | -32.8 |
| | $2OH^-$ | $2H_2O$ | $H_3O^+$ |

Table S3. Condensation reaction energies (in kcal/mol) between dimers (rows) $[Mo^V{}_2O_3(OH)_4(H_2O)(CH_3COO)]^-$ or $[Mo^V{}_2O_3(OH)_2(H_2O)_2(CH_3COO)]^-$ and pentagonal fragments (columns) $[Mo^V{}_2O_8H_6(CH_3COO)]^-$ as function of the protonation degree. The inner labels indicate the products obtained upon condensation.

We followed the same procedure taking into account different structures for dimers and pentagons. These structures were obtained from Carl-Parrinello molecular dynamics simulations performed on the pentagonal unit $[Mo_6O_{21}]^{6-}$ and on dimmers with stoichiometry $[Mo^V{}_2O_8H_6(CH_3COO)]^-$. The structures suggested by these simulations are a pentagon with three protons $[Mo_6O_{18}(OH)_3]^{3-}$ and two kinds of dimers: $[Mo^V{}_2O_3(OH)_4(H_2O)(CH_3COO)]^-$ and $[Mo^V{}_2O_3(OH)_2(H_2O)_2(CH_3COO)]^-$.

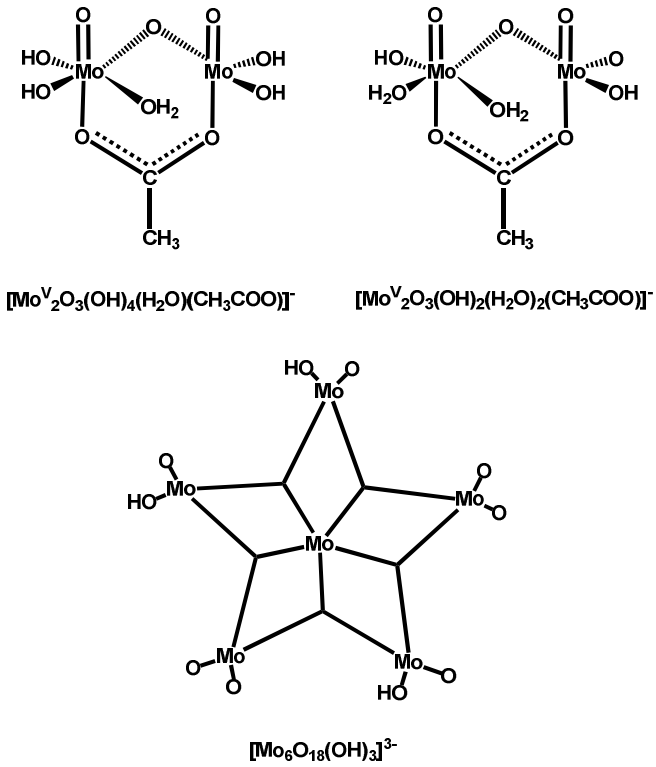


Figure S9. Scheme of the dimers and pentagonal unit obtained with Carl-Parrinello MD simulations and used to study the condensation process in Table S3.

We computed the different condensation possibilities leaded by those structures. We considered the four possibilities leaded by the two types of linkers. In the case of the pentagon, we have two possibilities for the binding site: the linker can be bonded to the pentagon through two oxygen sites or one oxygen and one hydroxyl group. Following the previous table trend, we considered also the possibility of having two consecutives hydroxyl groups, changing the order of the terminal groups one of the Mo atoms. We optimized this structured starting from the one obtained by Carl-Parrinello molecular dynamics simulations. The results show the structure with two consecutives hydroxyl groups is just 0.23 eV less stable than the proposed from molecular dynamics simulation. So we decided to include this structure in our studies.

These results are collected in Table S3 and reproduce the same trends that in the previous table. As the number of protons increases, the condensation energies become lower. The most favorable cases are the bottom-right ones, corresponding to condensations having four protons in all, giving water as product. These results are in perfect agreement with the previous ones. The different energy ranges presented on both tables can be explained in terms of the differences in the studied structures. Even if in both cases condensation takes place between a pentagon and a dimer, the structures used in the simulations present different geometries and charge.

We conclude that the protonation degree of the dimer and the pentagon are critical to the condensation occurs. Therefore, this condensation is very pH dependent and it seems more favorable at high pH.

**Modelling the $Mo_{132}$ Raman Spectrum Evolution**

Vibrational harmonic frequencies and Raman intensities were computed numerically from two-point single point calculations. For the reduced species $[Mo_7O_{24}]^{7-}$, since Raman intensities are not available in ADF for unrestricted determinants, Gaussian09[15] at an equivalent DFT level (BPV86) basis sets (6-311G* for O, LANL2TZ for Mo), and PCM solvent model were considered. At that level, G09 and ADF gave fully equivalent results for $[Mo_7O_{24}]^{6-}$.

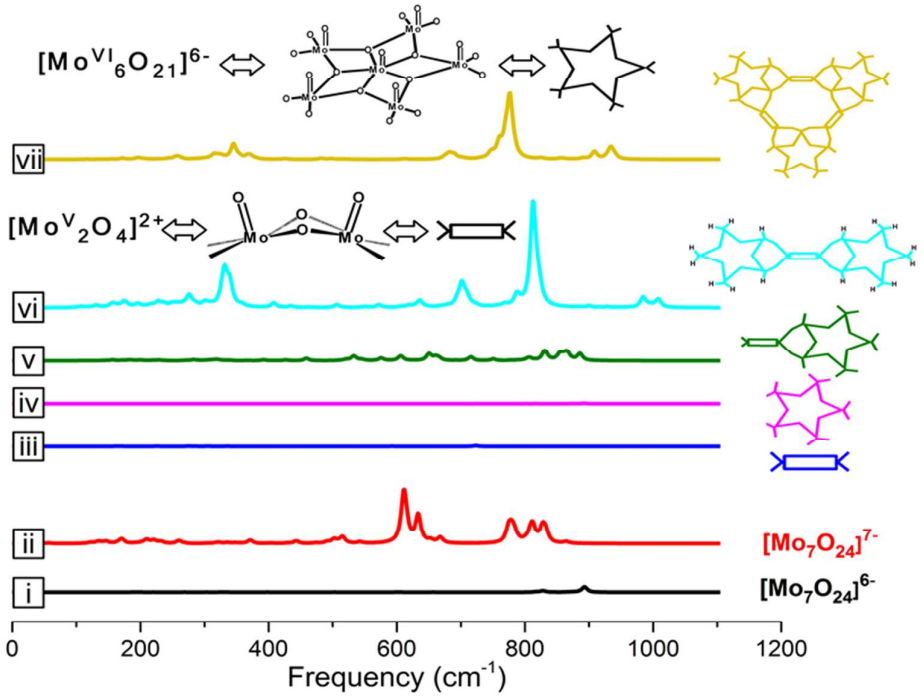


Figure S10. Computed Raman spectra for several $Mo_nO_m$ species. Intensities in $Ang^4$/amu units. Note that since the intensity scale covers 5 orders of magnitude, some spectra look flat (see text).

Figure S10 collects the computed Raman spectra for several systems, all represented at the same intensity scale. Full details of each spectrum, numerical values and assignment of all the most intense normal modes is provided in the Supporting Information.

For $[Mo_7O_{24}]^{6-}$, a, the most intense main peaks lie between 800 and 900 $cm^{-1}$, and those arise from the Mo–O stretching vibrations of the terminal oxygen atoms. Both signals present relatively low intensities. The anti-symmetric one at 830 $cm^{-1}$ is less intense (547 $Ang^4$/amu) than the signal at 893 $cm^{-1}$ (intensity 3300 $Ang^4$/amu), which correspond to the symmetric combination. At lower frequencies, very low peaks not distinguishable in Figure S10 at around 300 $cm^{-1}$, we found the terminal oxygen vibrational modes. These results, although not distinguishable in Figure S10, are in full agreement with experimental findings.

After reduction, $[Mo_7O_{24}]^{7-}$ (ii), the computed Raman spectrum shows active signals in two main regions. In the first set, around 615 $cm^{-1}$ (35000 $Ang^4$/amu), we found bending and stretching vibrations of the non terminal oxygen atoms. The second set comprises signals from 774 to 832 $cm^{-1}$ (15000 $Ang^4$/amu) assigned to stretching of the terminal oxygens. Compared to the non-reduced species, the experimental spectrum shows the appearance of signals below 850 $cm^{-1}$ that could assigned to the computed down shift of terminal oxygens in ii.

Spectra of species iii and iv, as they are shown in Figure S10, are apparently Raman silent (see below). iii corresponds to a linker-like $Mo^V{}_2O_4$ species, with terminal oxygens. This spectrum has a main peak at 723 $cm^{-1}$ (500 $Ang^4$/amu) corresponding to the terminal oxygens symmetric stretching. The presence of bridging ligands in the linker ($HCOO^-$, $CH_3COO^-$, $HCO_3^-$, $CO_3^{2-}$, $SO_4^{2-}$) does not affect the spectrum in significant manner. In some cases low intensity peaks appear around 300 $cm^{-1}$ caused by bridging oxygens, and also due to the ligand atoms themselves.

iv is the pentagonal moiety building block $[Mo^{VI}{}_6O_{21}]^{6-}$, as shown in the inset in Figure S10, that shows a main peak at 892 $cm^{-1}$ (intensity 300) that arise from terminal oxygen atoms symmetric stretching vibrational modes.

Spectra v, vi and vii correspond to different pentagon/linker assemblies built by binding pentagonal building blocks $[Mo^{VI}{}_6O_{21}]^{6-}$ and linkers $[Mo^V{}_2O_4]^{2+}$.

In v, there is a set of new peaks around 650 $cm^{-1}$. The peak with highest intensity (5000 $Ang^4$/amu) corresponds with the bridging oxygen scissoring and the pentagon non terminal oxygens bending. Also, we found as well the band around 850 $cm^{-1}$ (6000 $Ang^4$/amu) due to terminal oxygen stretching.

In vi, terminal oxygen atoms were capped with hydrogens. First, we have two peaks due to bridging oxygen wagging modes at 275 $cm^{-1}$ (8000 $Ang^4$/amu) and 330 (25000 $Ang^4$/amu). At 700 $cm^{-1}$ we found a peak due to bridging oxygen symmetric stretching (15000 $Ang^4$/amu). The main peak (60000 $Ang^4$/amu) is at 813 $cm^{-1}$ and corresponds to the pentagon/linker bridging oxygens symmetric stretching. Finally, around 1000 $cm^{-1}$, we found a set of peaks due to the terminal oxygens stretching (6000 $Ang^4$/amu).

Lastly, system vii is a model of a $Mo_{132}$ pore framework. It is formed by three pentagons joined by three linkers. In this case, we found a peak at 345 $cm^{-1}$ (1000 $Ang^4$/amu) caused by the pentagon non terminal oxygens bending. Around 690 $cm^{-1}$, we have several pentagon non terminal oxygens bending vibrations, which, together, have an intensity of 10000 $Ang^4$/amu. The main peak (33400 $Ang^4$/amu) is at 777 $cm^{-1}$ and is due to the pore-linker bridging oxygens. Finally, around 920 $cm^{-1}$ there are to peaks due to the terminal oxygens stretching (2000 and 5000 $Ang^4$/amu).

**Additional experiments**

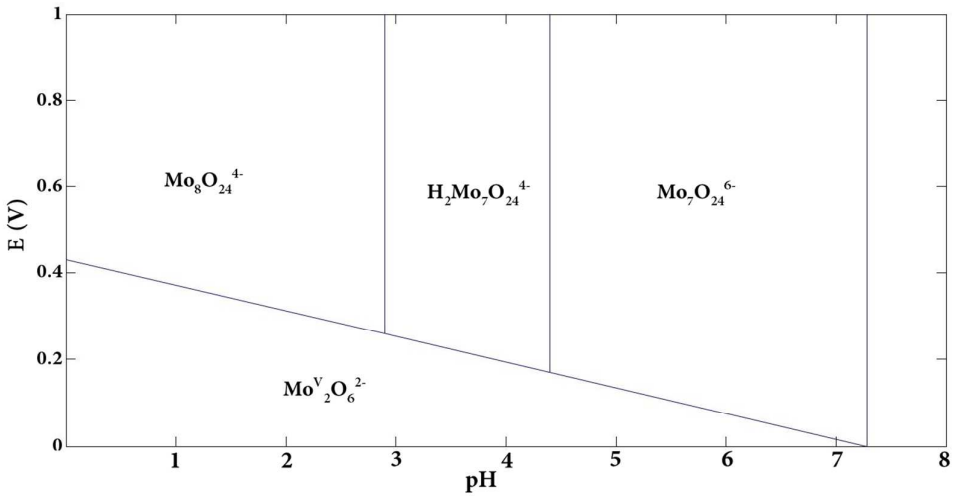


Figure S11. Simplified potential-pH diagram of formation of $Mo_{132}$ from heptamolybdate. Standard thermodynamic values for all species have been taken from reference [16].

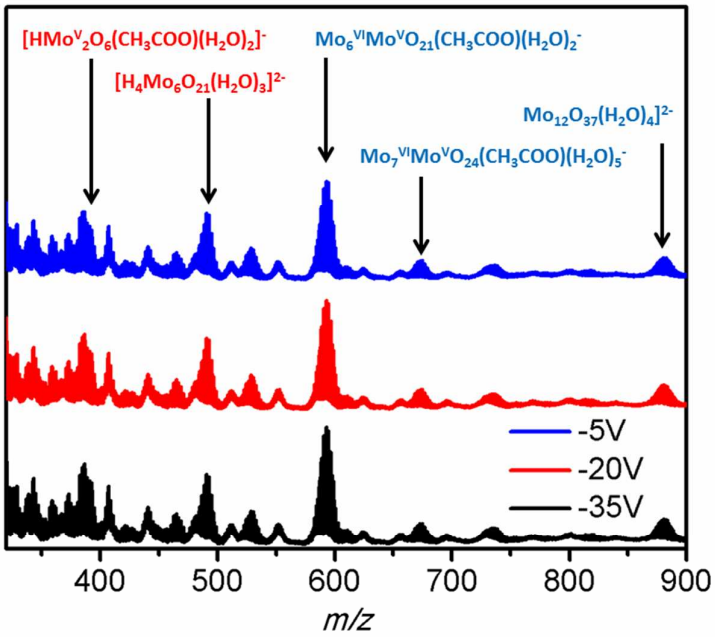


Figure S12. ESI-MS spectra of the solution after complete reduction at three different voltages viz., -5V, -20V and -35V show similar kind of spectrum at each voltages eliminating the presence of any voltage induced artifact[17]

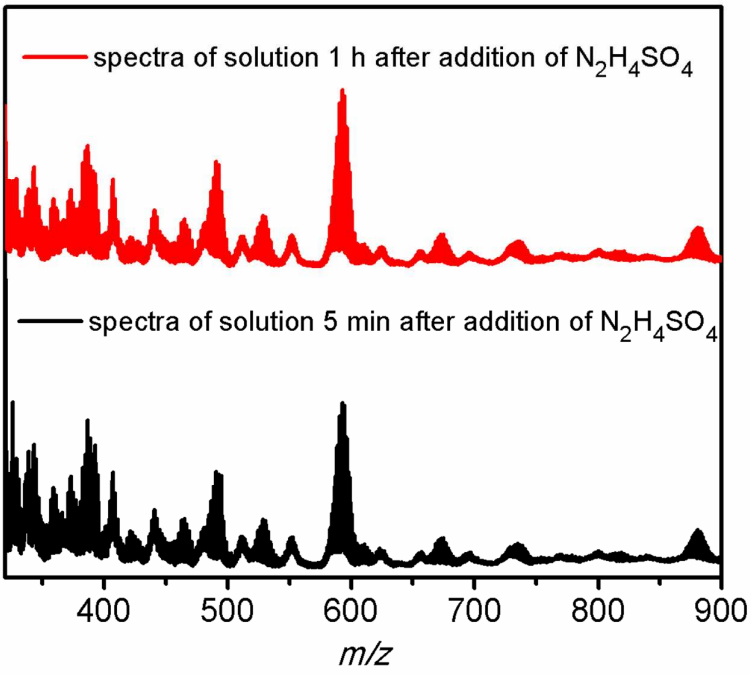


Figure S13. ESI-MS spectra of the reduced solution at two different time interval, after 5 min and after 1h of addition of hydrazine sulphate showing similar kind of spectra in both cases

Before acquiring the individual ESI-MS of each of the steps, we have provided sufficient time after addition of reagents to make sure that equilibrium has been established in solution. While acquiring the spectra, we have seen that within a few minutes equilibrium is established and no new peak appears after that. This is shown in Figure S13 considering the reduction step of the molybdate where spectrum of solution is taken five minutes after the addition of reducing agent and compared with spectrum acquired one hour after addition. No new peak has been noticed to appear even after keeping the solution for hours and the intensities of the peaks are also almost identical.

**References**


1. CPMD, IBM Corp.: Armonk, NY, 1990-2006; MPI für Festkörperforschung: Stuttgart 1997–2001.

2. Troullier, N.; Martins, J. L., *Phys. Rev. B* **1991**, *43*, 1993–2006.

3. Kachmar, A.; Bénard, M.; Rohmer, M. M.; Boero, M.; Massobrio, C., *J. Phys. Chem. A* **2009**, *113*, 9075–9079.

4. Becke, A. D., *Phys. Rev. A* **1988,** *38*, 3098-3100.

5. Perdew, J. P., *Phys. Rev. B* **1986,** *33*, 8822-8824.

6. Perdew, J. P., *Phys. Rev. B* **1986,** *34*, 7406-7406.

7. Car, R.; Parrinello, M., *Phys. Rev. Lett.* **1985**, *55*, 2471–2474.

8. Nosé, S., *J. Chem. Phys.* **1984**, *81*, 511–519.

9. Nosé, S., *Mol. Phys.* **1984**, *52*, 255–268.

10. Hoover, W. G., *Phys. Rev. A* **1985**, *31*, 1695–1697.

11. Baerends, E. J. A., J.; Bérces, A.; Bo, C.; Boerrigter, P. M.; Cavallo, L.; Chong, D. P.; Deng, L.; Dickson, R. M.; Ellis, D. E.; Faassen, M. v.; Fan, L.; Fischer, T. H.; Guerra, C. F.; Gisbergen, S. J. A. v.; Groeneveld, J. A.; Gritsenko, O. V.; Grüning, M.; Harris, F. E.; Hoek, P. v. d.; Jacobsen, H.; Jensen, L.; Kessel, G. v.; Kootstra, F.; Lenthe, E. v.; McCormack, D. A.; Michalak, A.; Osinga, V. P.; Patchkovskii, S.; Philipsen, P. H. T.; Post, D.; Pye, C. C.; Ravenek, W.; Ros, P.; Schipper, P. R. T.; Schreckenbach, G.; Snijders, J. G.; Sola, M.; Swart, M.; Swerhone, D.; Velde, G. t.; Vernooijs, P.; Versluis, L.; Visser, O.; Wang, F.; Wezenbeek, E. v.; Wiesenekker, G.; Wolff, S. K.; Woo, T. K.; Yakovlev, A. L.; Ziegler, T., Amsterdam Density Functional Program; http://www.scm.com.

12. Vanlenthe, E.; Baerends, E. J.; Snijders, J. G., *J. Chem. Phys.* **1993,** *99*, 4597-4610.

13. Vanlenthe, E.; Baerends, E. J.; Snijders, J. G., *J. Chem. Phys.* **1994,** *101*, 9783-9792.

14. Klamt, A., *J. Phys. Chem.* **1995,** *99*, 2224-2235.

15. Frisch, M. J.; Trucks, G. W.; Schlegel, H. B.; Scuseria, G. E.; Robb, M. A.; Cheeseman, J. R.; Scalmani, G.; Barone, V.; Mennucci, B.; Petersson, G. A.; Nakatsuji, H.; Caricato, M.; Li, X.; Hratchian, H. P.; Izmaylov, A. F.; Bloino, J.; Zheng, G.; Sonnenberg, J. L.; Hada, M.; Ehara, M.; Toyota, K.; Fukuda, R.; Hasegawa, J.; Ishida, M.; Nakajima, T.; Honda, Y.; Kitao, O.; Nakai, H.; Vreven, T.; Montgomery Jr., J. A.; Peralta, J. E.; Ogliaro, F. o.; Bearpark, M. J.; Heyd, J.; Brothers, E. N.; Kudin, K. N.; Staroverov, V. N.; Kobayashi, R.; Normand, J.; Raghavachari, K.; Rendell, A. P.; Burant, J. C.; Iyengar, S. S.; Tomasi, J.; Cossi, M.; Rega, N.; Millam, N. J.; Klene, M.; Knox, J. E.; Cross, J. B.; Bakken, V.; Adamo, C.; Jaramillo, J.; Gomperts, R.; Stratmann, R. E.; Yazyev, O.; Austin, A. J.; Cammi, R.; Pomelli, C.; Ochterski, J. W.; Martin, R. L.; Morokuma, K.; Zakrzewski, V. G.; Voth, G. A.; Salvador, P.; Dannenberg, J. J.; Dapprich, S.; Daniels, A. D.; Farkas, Ã. d. n.; Foresman, J. B.; Ortiz, J. V.; Cioslowski, J.; Fox, D. J., *Gaussian 09*, Gaussian, Inc.: Wallingford, CT, USA, **2009**.

16. Czack, G.; Kirschstein, G.; Haase, V.; Fleischmann, W. D.; Gras, D., *Mo Molybdenum: Physical Properties, Part 2. Electrochemistry*, Springer Berlin Heidelberg, **2013**.

17. Ma, M. T.; Waters, T.; Beyer, K.; Palamarczuk, R.; Richardt, P. J. S.; O'Hair, R. A. J.; Wedd, A. G., I*norg. Chem.* **2009**, *48*, 598–606.